Industrial Chemistry & Materials

ROYAL SOCIETY OF CHEMISTRY

PAPER

View Article Online
View Journal

Cite this: DOI: 10.1039/d5im00252d

Theoretical insights of nickel-based dual-metal atoms supported on C_2N sheets for urea electrooxidation

Xingqun Zheng,[a] Yuhan Mei,[b] Yi Zeng,[c] Qingsong Hua*[c] and Shun Lu *[d]

The electrocatalytic urea oxidation reaction (UOR) enables energy-saving hydrogen production and waste degradation but requires efficient catalysts due to its complex, sluggish 6-electron transfer mechanism. In this study, we designed a series of stable 3d transition metal heterometal atom pairs (TMNi, TM refers to Sc, Ti, V, Cr, Mn, Fe, Co, Ni, Cu, or Zn) supported on the C_2N substrate as UOR catalysts, systematically investigating their potential to enhance the activity of Ni_2/C_2N. Among these, $CrNi/C_2N$ displayed a superior capability to lower the limiting potential of the UOR compared to $CuNi/C_2N$ and Ni/C_2N. The enhanced catalytic $CrNi/C_2N$ system primarily stems from the stronger TM–Ni interactions, notable differences in charge distribution, more localized electronic states, and a higher d-band center associated with $CrNi/C_2N$ relative to $CuNi/C_2N$ and Ni_2/C_2N. These attributes not only ensure the stability of the well-dispersed CrNi pairs on C_2N but also amplify the ability of the active center to adsorb and activate reaction intermediates. Moreover, $CrNi/C_2N$ demonstrates good selectivity for the UOR by exhibiting reduced susceptibility to forming NO_2 by-products and undergoing the competing oxygen evolution reaction. This theoretically driven work identifies $CrNi/C_2N$ as the top-performing UOR dual-metal-atom catalysts, combining 0.99 V limiting potential with selective N_2 generation through electronic structure modulation, offering guidance for advanced catalyst design through the strategic use of transition metal heterometal atom pairs.

Received 15th September 2025,
Accepted 24th October 2025

DOI: 10.1039/d5im00252d

rsc.li/icm

Keywords: Urea oxidation reaction; C_2N; Dual-atom catalyst; Nickel-based compounds; DFT calculations.

1 Introduction

Urea, a nitrogen-rich compound, is prevalently found in domestic sewage, industrial wastewater and agriculture wastes. The degradation of urea in these wastewaters is one of the useful methods that prevent urea from transferring into harmful nitrogen oxides that pollute the environment.[1–3] In recent years, the coupling of the urea oxidation reaction (UOR) with the hydrogen evolution reaction in an electrolytic cell has garnered significant interest.[4,5] This method offers a relatively low theoretical potential of 0.37 V *vs.* RHE, which is 0.86 lower than that of the anodic oxygen evolution reaction (OER) in water electrolysis (1.23 V). UOR not only facilitates the degradation of urea-containing waste with minimal energy consumption but also generates high-value hydrogen, thereby contributing to both green energy production and environmental protection. Nevertheless, the UOR involves a sluggish 6-electron transfer step and the formation of multiple reaction intermediates, resulting in a rather complex reaction mechanism. Hence, the development of highly efficient catalysts is crucial for facilitating the efficient progress of the UOR. Currently, the research on UOR catalysts mainly focuses on Ni-based materials, such as nickel-based alloys, nickel-based metal compounds (such as Ni-based oxides, phosphides, sulfides, *etc.*).[6–10] Despite the advantages of certain UOR activity, good conductivity, low cost, and easy accessibility of these materials, the UOR activity on these materials is still restricted by unclear active sites, ambiguous catalytic mechanism, and insufficient material stability.[11,12] Developing Ni-based materials with high activity, stability, and clear active sites and elucidating the catalytic mechanism remain the main tasks in the current research on UOR catalysts.

In the past decade, the emergence of single-atom catalysts (SACs) has aroused great interest due to their high atomic utilization efficiency and excellent catalytic activity. Researchers have combined different metal single atoms and various types of support materials to form SACs for catalyzing

[a] *School of Safety Science and Engineering, Chongqing University of Science and Technology, Chongqing, 401331, China*
[b] *Department of Chemical and Biomolecular Engineering, North Carolina State University, Raleigh, NC 27695, USA*
[c] *School of Physics and Astronomy, Beijing Normal University, Beijing 100875, China. E-mail: q.hua@bnu.edu.cn*
[d] *Chongqing Institute of Green and Intelligent Technology, Chinese Academy of Sciences, Chongqing 400714, China. E-mail: lushun@cigit.ac.cn*

various electrocatalytic reactions.[13–15] Despite promising prospects, SACs usually have simple structures and lack coordinated active sites, which prevent them from breaking the linear relationship between the adsorption energy of reaction intermediates, activating the complex intermediates, and surpassing the inherent electrocatalytic performance limitations, such as activity, stability and high selectivity.[16,17] To address this issue, a more promising strategy is to introduce a second metal atom on the support substrate to form dual-metal-atom catalysts (DACs). DACs can combine the advantages of two metal atoms and introduce atomic-level synergistic interactions, which are expected to break the theoretical limits of SACs.[18,19] For DACs, the substrate interacts with metal atoms through chemical bonds, stabilizing the metal atoms and altering their electronic structure.[20,21] Therefore, in addition to the type and inherent properties of the metal atom, the substrate for DACs is equally important.

Different from the commonly utilized graphene-based materials, C_2N monolayers, as a prominent two-dimensional material, feature a uniform nitrogenated pore structure. The edges of these pores, rich in sp^2-bonded nitrogen atoms, can effectively anchor metal atoms or clusters and hinder their diffusion or aggregation.[22] As a result, C_2N has proven to be an excellent substrate for accommodating dual atoms. Various metal atoms have been anchored onto the C_2N substrate to form catalysts with atomically-doped pairs, such as Sc_2/C_2N, Ti_2/C_2N, and Cu_2/C_2N, which have been developed for catalyzing various electrocatalytic reactions, including hydrogen evolution, nitrogen reduction, oxygen reduction, and hydrazine oxidation.[23–26]

Although there has been limited research on the use of C_2N-supported metal atoms for the UOR, our previous studies have confirmed that Ni single atoms loaded on C_2N to form Ni/C_2N exhibit certain UOR activity.[27] Building upon this, by introducing a second Ni atom into the pores of C_2N to design the dual-atom catalyst Ni_2/C_2N, it can provide dual anchoring sites for N-containing intermediates, thus facilitating the adsorption and transformation of nitrogen-containing intermediates and ultimately enhancing UOR activity.[27] However, compared to some Ni-based catalysts, Ni_2/C_2N still shows certain activity deficiencies. One approach to enhancing the activity of dual-atom catalysts is to achieve atom pair heterogenization by introducing a second metal atom, thereby forming catalysts that effectively improve the catalytic activity. For instance, Li *et al.* synthesized CuCo DACs which exhibit strong synergistic interactions between asymmetrically deployed CuC_4 and CoN_4 sites, resulting in a significantly polarized charge distribution.[28] This leads to enhanced capabilities of the catalyst in substrate adsorption and O_2 activation, demonstrating better performance for the oxidative esterification of aromatic aldehydes than the single active component. Ren *et al.* synthesized a Ni/Fe–N–C catalyst with Ni–Fe pairs, where the synergy between Ni and Fe reduced the energy barriers for *COOH formation and *CO desorption, facilitating CO_2 reduction.[29] For the purpose of breaking through the stubborn restriction of scaling relations on SAC catalysts, Wang *et al.* designed $CuCr/C_2N$ and $CuMn/C_2N$ that show low limiting potentials of −0.37 V and −0.32 V, respectively, for CO_2 reduction to CH_4.[30] Thereby, a similar strategy can be applied to enhance the UOR activity of Ni_2/C_2N and further clearly understand the microscopic reaction mechanisms and fundamental factors that determine the catalytic activity, but still remains unexplored.

Based on the above discussion, this study aims to introduce 3d transition metal atoms into the Ni_2/C_2N system to form TM–Ni/C_2N catalysts containing TM–Ni hetero-atom pairs. The potential of TM atoms to enhance the UOR activity of Ni_2/C_2N is investigated using density functional theory calculations along with the selection of heteroatomic pairs with optimal activity. Furthermore, by analyzing the catalytic mechanism, identifying key intermediates, and examining the electronic structures of metal atom pairs within TM–Ni/C_2N along with the interactions of these active sites with key intermediates, the fundamental reasons behind the promotion of UOR activity facilitated by the optimal TM–Ni/C_2N catalysts are explored. Finally, the selectivity and stability of the optimal catalysts are evaluated by excluding the possibility of catalytic side reactions and assessing the kinetic stability of the catalysts.

2 Results and discussion

2.1 The structure and stability analysis of $TMNi/C_2N$

Based on Ni/C_2N and Ni_2/C_2N structures constructed in previous work,[27] we incorporated another TM atom into Ni/C_2N or substituted a Ni atom in Ni_2/C_2N with another TM atom, where TM refers to 3d transition metal atoms such as Sc, Ti, V, Cr, Mn, Fe, Co, Ni, Cu, and Zn, as illustrated in Fig. 1a. This resulted in the formation of TMNi dual atoms anchored within the hole of C_2N. Both TM and Ni atoms tend to bond with three surrounding N atoms, forming three TM–N bonds, while TM–Ni bonds are established between TM and Ni through the overlap of their valence orbitals. To assess the thermodynamic stability of the $TMNi/C_2N$ system, we calculated two types of binding energies with consideration of two scenarios during the synthesis process: the sequential anchoring of TM following Ni on C_2N and the simultaneous anchoring of TMNi onto the C_2N substrate. The former one is the binding energy of TM on Ni/C_2N, denoted as $E_{b(TM)}$, according to the following equation:

$$E_{b(TM)} = E_{TMNi/C_2N} - E_{Ni/C_2N} - E_{TM} \quad (1)$$

The latter one is the binding energy of TMNi adding on the hollow of C_2N ($E_{b(TMNi)}$) which was defined as:

$$E_{b(TMNi)} = E_{TMNi/C_2N} - E_{C_2N} - E_{TMNi} \quad (2)$$

Here, E_{TMNi/C_2N}, E_{Ni/C_2N}, E_{TM}, E_{TMNi} and E_{C_2N} are the energies of $TMNi/C_2N$, Ni/C_2N, single TM atom, TMNi atom

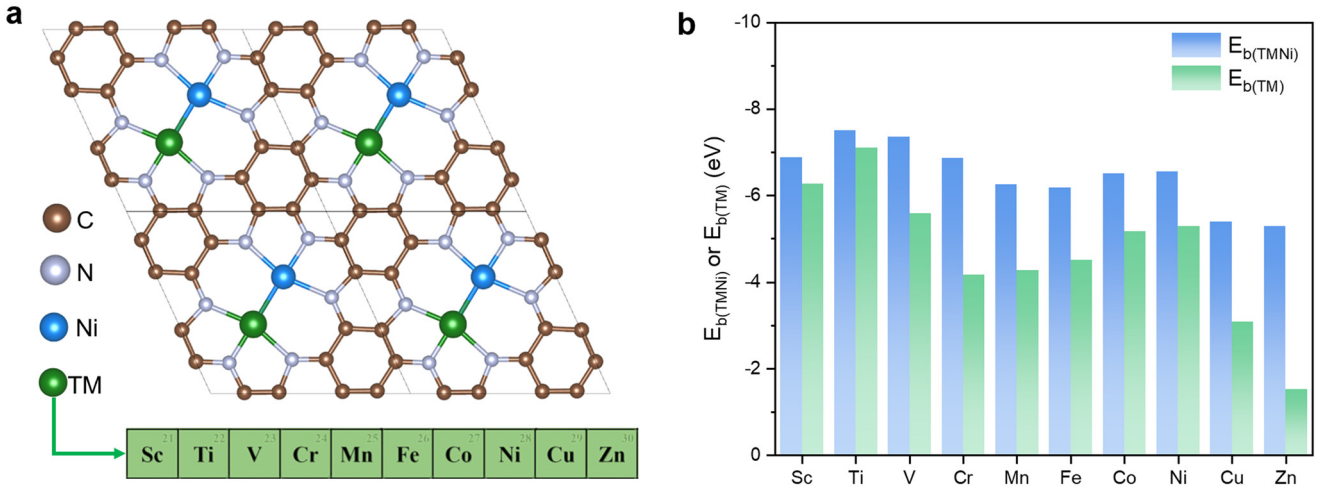

Fig. 1 (a) The structure of TMNi/C_2N. (b) The binding energies of TMNi ($E_{b(TMNi)}$) on C_2N and TM ($E_{b(TM)}$) on Ni/C_2N.

pair and C_2N, respectively. The results of these binding energies are shown in Fig. 1b. Notably, all calculated values of $E_{b(TMNi)}$ and $E_{b(TM)}$ are negative, suggesting that either the TMNi pair or TM can be stably anchored in the not fully occupied hole of C_2N. Besides, $E_{b(TMNi)}$ is significantly more negative than $E_{b(TM)}$. This observation indicates that the abundance of N atoms on the edge of the hole of C_2N facilitates the anchoring of the TMNi pair.

2.2 Screen of the promising TMNi/C_2N for UOR

To identify the TMNi/C_2N systems with optimal UOR activity, we need to determine the catalytic pathways first. Based on prior research and the literature,[7,27] we identified two pathways as depicted in Fig. 2a: one pathway, referred to as the O_{ter} pathway, primarily involves the adsorption of intermediates mainly *via* O–TM interactions, while the other, referred to as the N_{ter} pathway, focuses on the adsorption of intermediates *via* N–TM interactions. In the two pathways, the adsorbed species dehydrogenate gradually, then experience C–N bond breakdown and N_2 formation, and finally CO oxidation to produce CO_2. Due to the presence of bimetallic sites, in the O_{ter} pathway, nitrogen-containing intermediates form metal–adsorbate bonds with both metal atoms mainly through O and N atoms. In contrast, the N_{ter} pathway involves the formation of chemical bonds with both metal atoms primarily through two N atoms.

Following this, we examined the adsorption ability of the TMNi site for urea molecules in both pathways by calculating the adsorption Gibbs free energy (ΔG_{ads}), and a positive value of ΔG_{ads} indicates that urea molecules can be spontaneously or easily adsorbed on active sites, while a negative value suggests the opposite. In Fig. 2b, urea tends to be adsorbed on a single metal atom *via* either an O–TM (O_{ter} adsorption structure) or a N–TM bond (N_{ter} adsorption structure) due to the saturated coordination of N in urea molecules. For one TMNi/C_2N, the O_{ter} adsorption structure exhibits a more negative ΔG_{ads} value than the N_{ter} structure, indicating better stability for the O_{ter} adsorption structure. Notably, the ΔG_{ads} values of urea adsorption on Ni_2/C_2N are positive for both adsorption configurations, whereas all other TMNi/C_2N systems yield more negative ΔG_{ads} values for urea adsorption. Except for Cu, all other TM variants result in negative ΔG_{ads}, indicating that urea can be spontaneously adsorbed on the corresponding TMNi/C_2N. Furthermore, the ΔG_{ads} value decreases as the TM employed occurs earlier in the periodic table, suggesting that introducing heterogeneous TM into the Ni/C_2N system can enhance urea adsorption.

Subsequently, we calculated the free energy changes (ΔG) for each step in both pathways and plotted the free energy profiles of each system (Fig. S1). We summarized the ΔG of the potential determining step (PDS) of all TMNi/C_2N systems, represented as ΔG_{PDS}, which corresponds to the maximum ΔG (ΔG_{max}) of each pathway. In Fig. 2c, except for TiNi/C_2N and MnNi/C_2N, all other TMNi/C_2N systems exhibit a lower ΔG_{PDS} for the N_{ter} pathway compared to the O_{ter} pathway, indicating a higher tendency for the N_{ter} pathway to occur. Taking Ni_2/C_2N as a reference, the ΔG_{PDS} values for the O_{ter} and N_{ter} pathways are 1.62 eV and 1.22 eV, respectively. In the case of the O_{ter} pathway, except for ZnNi/C_2N, all other TMNi/C_2N systems exhibit ΔG_{PDS} values lower than that of Ni_2/C_2N. Notably, the introduction of Ti, Cr, and Cu (with ΔG_{PDS} values of 1.18, 1.09, and 1.18 eV, respectively) significantly reduces the ΔG_{PDS} for the O_{ter} pathway on TMNi/C_2N, suggesting that these transition metals can effectively facilitate the UOR through the O_{ter} pathway. Regarding the N_{ter} pathway, only certain TM atoms, like V, Cr, Fe, and Cu, successfully lower the ΔG_{PDS} compared to Ni_2/C_2N, where V, Cr, and Cu especially contribute ΔG_{PDS} of TMNi/C_2N of 1.11 eV, 0.99 eV, and 1.08 eV, respectively. This indicates that the introduction of V, Cr or Cu can promote the N_{ter} pathway more effectively. Considering the ΔG_{PDS} of both pathways, Cr and Cu demonstrate a capacity to decrease the ΔG_{PDS} for Ni_2/C_2N in both pathways, establishing them as effective alternatives among the chosen 3d transition metals to replace one Ni in

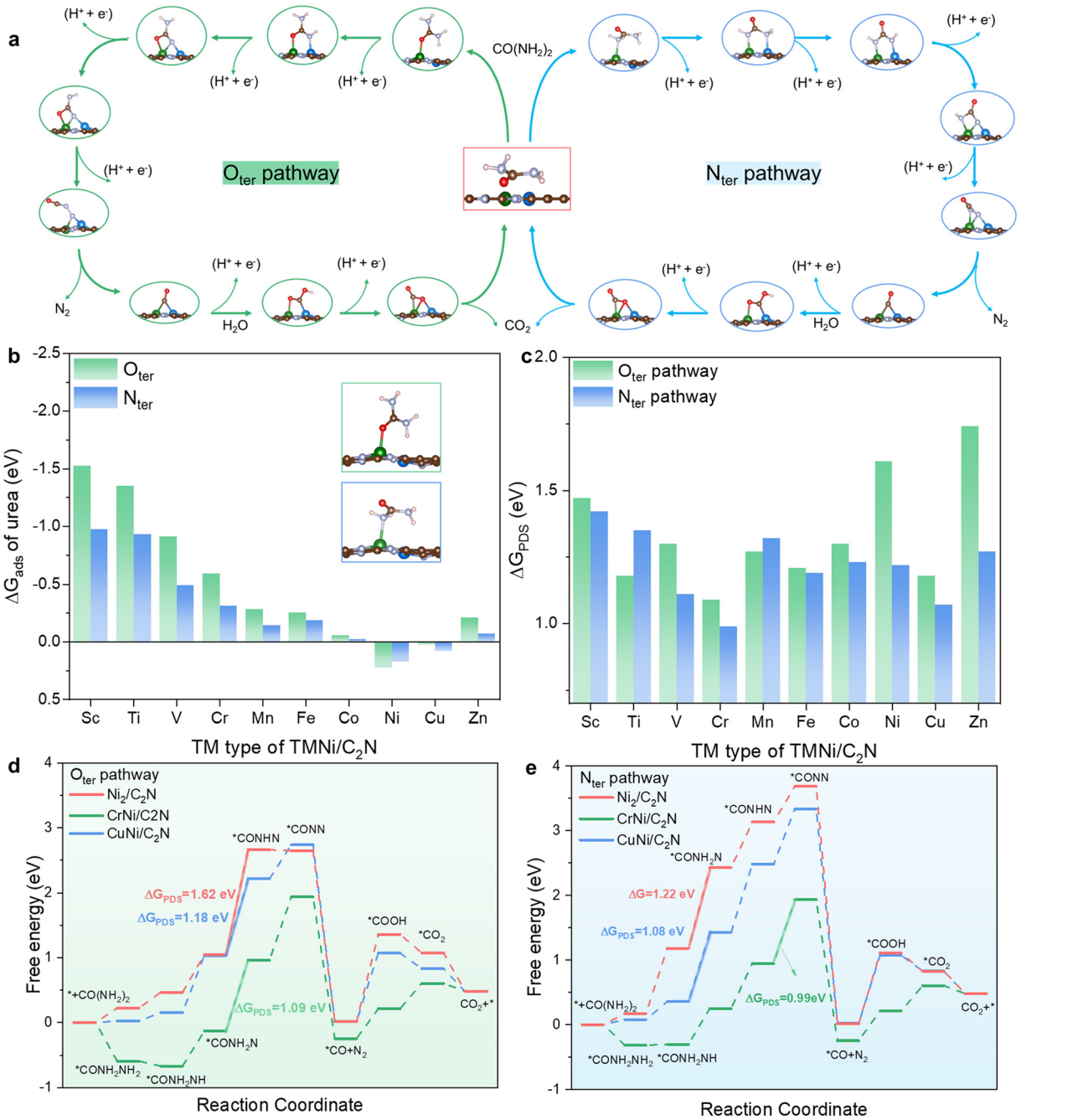

Fig. 2 (a) The schematic diagram of the O_{ter} pathway and N_{ter} pathway. (b) The urea adsorption free energy (ΔG_{ads}) on $TMNi/C_2N$ and the insets are the adsorption model of urea with O_{ter} (green) and N_{ter} (blue) structures, respectively. (c) The free energy change of potential determining steps (ΔG_{PDS}) of the two pathways on $TMNi/C_2N$. (d and e) The free energy diagrams of the O_{ter} and N_{ter} pathway on Ni_2/C_2N, $CrNi/C_2N$ and $CuNi/C_2N$, respectively.

the Ni_2/C_2N or to add in the hole of Ni/C_2N and thereby promote the UOR.

Next, the UOR free energy diagrams for $CrNi/C_2N$ and $CuNi/C_2N$ are compared with that for Ni_2/C_2N to explore the differences in the UOR mechanism and activity among these systems. The activation and deprotonation of urea, or the oxidation of the *CO intermediate, are often regarded as key steps for the UOR.[31,32] As shown in Fig. 2d and e, for the O_{ter} pathway, urea adsorption, activation, and all deprotonation steps on the active sites of Ni_2/C_2N and $CuNi/C_2N$ are endothermic processes, while on $CrNi/C_2N$, the urea adsorption and first proton desorption steps are exothermic, suggesting that $CrNi/C_2N$ is more favorable for initiating urea oxidation. Additionally, during the *CO oxidation stage (*i.e.*, *CO → *COOH), $CrNi/C_2N$ requires less energy than Ni_2/C_2N and $CuNi/C_2N$, making it more favorable for *CO oxidation. For the PDS of these three systems, the third proton desorption step (*$CONH_2N$ → *CONHN) prevails, and based on their ΔG_{PDS} values, the activity follows the sequence $CrNi/C_2N$ > $CuNi/C_2N$ > Ni_2/C_2N. Furthermore, compared to

Ni_2/C_2N, the limiting potential $U_{limiting}$ (calculated as $U_{limiting} = \Delta G_{PDS}/e$) for $CrNi/C_2N$ and $CuNi/C_2N$ is reduced by 0.53 V and 0.44 V, respectively, indicating the higher activity of $CrNi/C_2N$ and $CuNi/C_2N$. Similarly, for the N_{ter} pathway, the $CrNi/C_2N$ exhibits catalytic characteristics analogous to those seen in the O_{ter} pathway, favoring urea adsorption, activation, and *CO oxidation. The PDS for the Ni_2/C_2N and $CuNi/C_2N$ corresponds to the second proton desorption step (*i.e.* $*CONH_2NH \rightarrow *CONH_2N$), whereas $CrNi/C_2N$ features the fourth proton desorption step (*i.e.* *CONHN → *CONN). The activity order remains $CrNi/C_2N > CuNi/C_2N > Ni_2/C_2N$, with $CrNi/C_2N$ and $CuNi/C_2N$ showing reduction in $U_{limiting}$ of 0.23 V and 0.14 V, respectively, compared to Ni_2/C_2N. Across both pathways, the subsequent deprotonation steps of nitrogen-containing intermediates in the $TMNi/C_2N$ systems remain critical to the overall reaction. Compared with Ni_2/C_2N, the presence of heterogeneous TM in $CrNi/C_2N$ or $CuNi/C_2N$ enhances the adsorption of nitrogen-containing intermediates, thereby reducing the energy change for key steps and ultimately improving catalytic activity. Besides, the UOR on $CrNi/C_2N$ or $CuNi/C_2N$ is more likely to experience the N_{ter} pathway than the O_{ter} pathway due to the lower $U_{limiting}$ of the N_{ter} pathway.

Given the critical role of the solvent in electrocatalytic reactions, it is essential to analyze whether the activity trends derived from vacuum calculations are held in a more realistic environment. To this end, we employed an implicit solvation model (VASPsol), which is widely used in theoretical studies of electrocatalysts,[33–36] to recalculate the free energy profiles of the N_{ter} pathway for three representative catalysts: $CrNi/C_2N$, $CuNi/C_2N$, and Ni_2/C_2N. In Fig. S2, the free energy diagram of the N_{ter} pathway with implicit solvation effect exhibits ΔG_{PDS} of 0.95, 1.03, and 1.28 eV for $CrNi/C_2N$, $CuNi/C_2N$, and Ni_2/C_2N, respectively. This clearly preserves the activity trend $CrNi/C_2N > CuNi/C_2N > Ni_2/C_2N$, which is identical to that concluded from our initial vacuum-phase screening. Although the absolute adsorption free energies of intermediates experience a shift of 0 to 0.5 eV compared to the vacuum case, the identity of the PDS and the relative activity trend remain unchanged. Therefore, the activity trend based on results of vacuum calculations is effective and reliable for identifying the most promising TM/C_2N candidate for efficient UOR.

To investigate the differences in catalytic activity between the selected optimal heterogeneous bimetallic atom catalysts and their corresponding homogeneous counterparts, we constructed models of Cr_2/C_2N and Cu_2/C_2N. Because $CrNi/C_2N$ and $CuNi/C_2N$ are more prone to converting urea into N_2 and CO_2 *via* the N_{ter} pathway, we mainly calculated the free energy changes of the UOR catalyzed by Cr_2/C_2N and Cu_2/C_2N along the N_{ter} pathway. As shown in Fig. S3, the PDS for Cr_2/C_2N corresponds to the step from *CONHN to *CONN, and for Cu_2/C_2N is *CONHNH to *CONHN, with ΔG_{PDS} values of 1.30 eV and 1.53 eV, respectively. These values are 0.31 eV and 0.45 eV higher than the corresponding ΔG_{PDS} for $CrNi/C_2N$ and $CuNi/C_2N$, respectively, verifying that $CrNi/C_2N$ and $CuNi/C_2N$ exhibit superior UOR activity compared to their homogeneous bimetallic counterparts. Thus, we focus on $CrNi/C_2N$ and $CuNi/C_2N$ and the origin of their activity in the next section.

2.3 Electronic structure analysis of promising $TMNi/C_2N$

The electronic structure of catalysts is crucial for the adsorption of intermediates and overall reaction. In this part, we explore the electronic structure starting from the intrinsic structural properties of the catalysts. We computed the charge density difference, Bader charge, and spin density of the bimetallic pair on C_2N, followed by calculating the density of states (DOS) and the crystal orbital Hamilton population (COHP) of the TMNi pair. The charge density difference diagrams in Fig. 3a and S4 show the difference of charge transfer between the three TMs (Ni, Cr and Cu) and Ni. It is clear that charge transfer occurs between Ni and these TM atoms, and compared with Ni_2/C_2N, the charge transfer between Cr and Ni is more significant, while the charge transfer between Cu and Ni is relatively weak. This indicates stronger interaction between the Cr–Ni pair among the three atomic pairs.

Further calculations of the surface Bader charge (Table 1, where positive values represent the loss of electrons, negative values represent the gain of electrons) reveal that the Cr (1.05 e) of $CrNi/C_2N$ and Cu (0.60 e) of $CuNi/C_2N$ possess more positive charges than their paired Ni atoms and the Ni (0.59 e) of Ni_2/C_2N. This suggests that Cr and Cu are more prone to transferring electrons to the system. Additionally, the introduction of Cr or Cu instead of Ni to the bimetallic atomic system leads to a partial transfer of electrons to its paired Ni atom, reducing its positive charge. Notably, Ni of $CrNi/C_2N$ exhibits the lowest Bader charge value (0.40 e) among the three systems, indicating that Ni accumulates more electrons from its TM in $CrNi/C_2N$ than the other two $TMNi/C_2N$, which is consistent with the results observed in the charge density difference (Fig. 3a). The clearly differentiated charge distribution between the Cr and Ni atoms in the $CrNi/C_2N$ system is advantageous for the adsorption and activation of intermediates.[37]

Moreover, the spin density in Fig. 3b shows almost negligible spin electron distribution on Ni_2/C_2N, indicating that the Ni_2 center is nonmagnetic. In contrast, the TMNi pairs in $CrNi/C_2N$ and $CuNi/C_2N$ exhibit significant spin electron distribution, with a more pronounced distribution around Cr. Calculations of the spin moments (Table 1) further confirm that Cr has significantly higher spin moments of 3.28 μ_B than Cu (0.57 μ_B). This also indicates that the spin electrons in $CrNi/C_2N$ are more localized. The distinctly localized spin moments on the Cr site of $CrNi/C_2N$ will facilitate the adsorption of intermediates.[24,38]

To investigate the electronic state distribution of the central metal atoms in the three systems, we calculated the

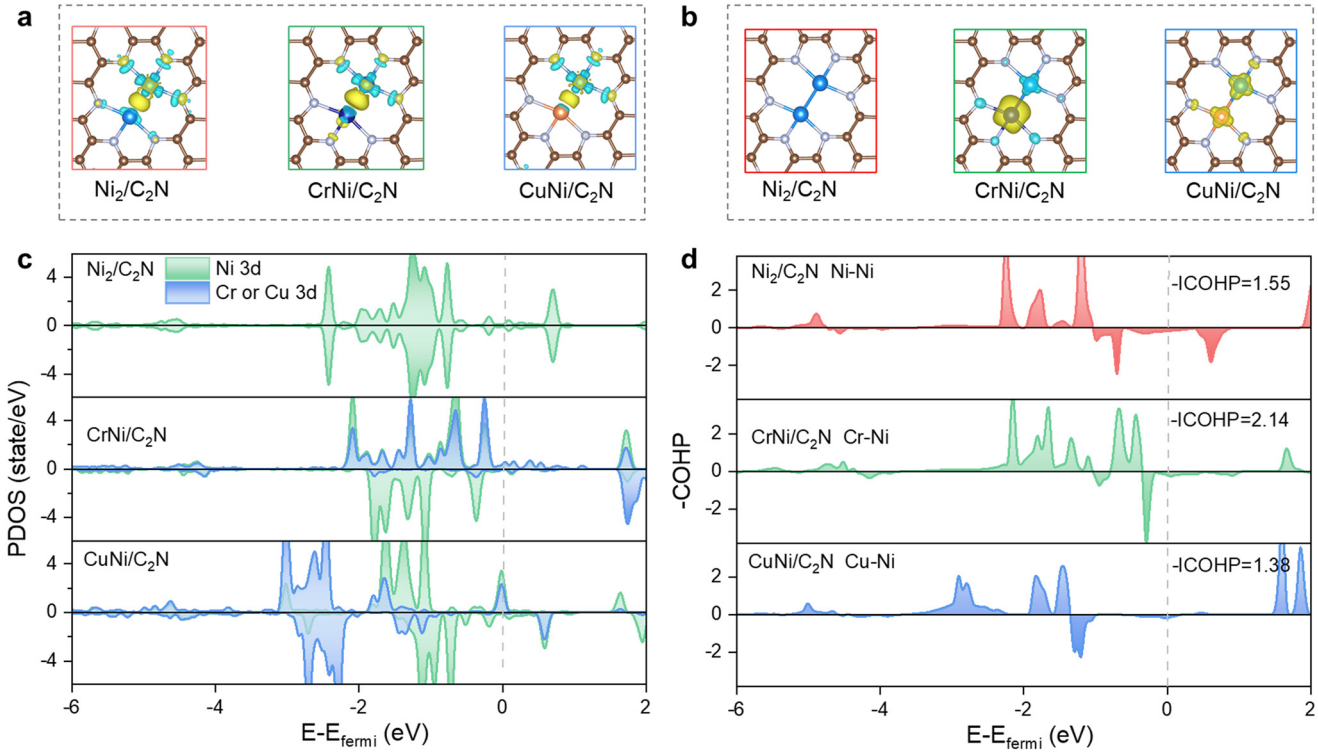

Fig. 3 (a) The charge density difference between Ni and TM/C_2N (*i.e.* the charge density of TMNi/C_2N minus that of Ni and TM/C_2N); the isosurface level is set as 0.01 e Å^{-3}, and yellow/blue represents charge accumulation/depletion. (b) The spin density of TMNi/C_2N with an isosurface level of 0.01 e Å^{-3}. (c) PDOS patterns of TM-3d orbitals for each TMNi/C_2N. (d) The crystal orbital Hamilton population (COHP) of the TMNi pair for each TMNi/C_2N.

projected density of states (PDOS) of the metal 3d orbitals (Fig. 3c). The central metal pair in Ni_2/C_2N exhibits a relatively symmetrical PDOS distribution with electronic states below the Fermi level primarily localized in the range of −2.5 to 1 eV, confirming its non-magnetic characteristics. In the CrNi/C_2N system, the spin-up and spin-down electronic states of Cr 3d and Ni 3d show a distinctly asymmetric distribution. The filled electronic states of Cr 3d are mainly localized in the spin-up portion with a narrow range of −2.2 to 0 eV, which confirms a more localized distribution of spin electrons on Cr. Furthermore, in CrNi/C_2N, there is significant PDOS resonance between Cr 3d and Ni 3d in the range of −2 to 0 eV, suggesting strong interactions between Cr and Ni. For CuNi/C_2N, the spin-up and spin-down electronic states of Cu 3d and Ni 3d also display an asymmetric distribution, with a more delocalized filling of electronic states (Cu 3d and Ni 3d are primarily distributed in the ranges of −3.5 to 1 eV and −3.5 to 0 eV, respectively). The resonance of Cu 3d and Ni 3d PDOS is confined to the energy regions around −3, −1.7, and 0 eV, indicating weaker interactions between Cu and Ni. Based on the PDOS, we computed the d-band center, shown in Table 1. Generally, the closer the d-band center is to the Fermi level (and the more positive it is), the more favorable it is for the adsorption of intermediates. When Cr or Cu replaces one Ni of Ni_2/C_2N, the d-band center of Ni shifts positively and thus can enhance the adsorption ability of the Ni site. Notably, Cr of CrNi/C_2N exhibits the highest positive d-band center (0.40 eV) among the three TM atoms, thus most favorably facilitating the adsorption of intermediates. Although Cu of CuNi/C_2N has the most negative d-band center among the three TM atoms, its 3d orbitals are more saturated with electrons, and its 3p orbital can also be considered to participate in bonding with intermediates. Therefore, we computed the Cu 3p band center, which yields a value of −0.47 eV, more positive than Ni 3p in Ni_2/C_2N (−1.03 eV), thereby also promoting the adsorption of intermediates. However, compared to CuNi/C_2N, CrNi/C_2N has a superior d-band center that can facilitate the adsorption of intermediates more efficiently.

Table 1 The Bader charge, spin moments and band center of Ni and TM in three TMNi/C_2N (TM = Ni, Cr and cu) systems

	Bader charge (e)		Spin moments (μ_B)		Band center (eV)		
Systems	Ni	TM	Ni	TM	Ni-3d	TM-3d	TM-3p
Ni_2/C_2N	0.59	0.59	0.00	0.00	−1.41	−1.41	−1.03
CrNi/C_2N	0.40	1.05	−0.21	3.28	−1.22	−0.40	−0.78
CuNi/C_2N	0.57	0.60	−0.27	0.57	−1.27	−2.52	−0.47

We then computed the COHP for TM–Ni pairs in all three systems and plotted the –COHP shown in Fig. 3d, with the purpose of exploring the bonding characteristics between TM

and Ni. The positive part of –COHP represents bonding contributions, while the negative part denotes antibonding contributions. It is evident that the antibonding contributions of the three TM–Ni pairs below the Fermi level are quite similar, but the bonding contributions for Cr–Ni are significantly greater than those for Ni–Ni and Cu–Ni, with Cu–Ni exhibiting the least bonding contribution. By integrating the –COHP, we obtained the –ICOHP values, where a more positive –ICOHP indicates a greater bonding contribution, thus stronger bonding. The order of –ICOHP for the TM–Ni interactions is Cr–Ni (2.14) > Ni–Ni (1.55) > Cu–Ni (1.38), confirming that Cr–Ni has the strongest interaction, followed by Ni–Ni, with Cu–Ni showing the weakest interaction.

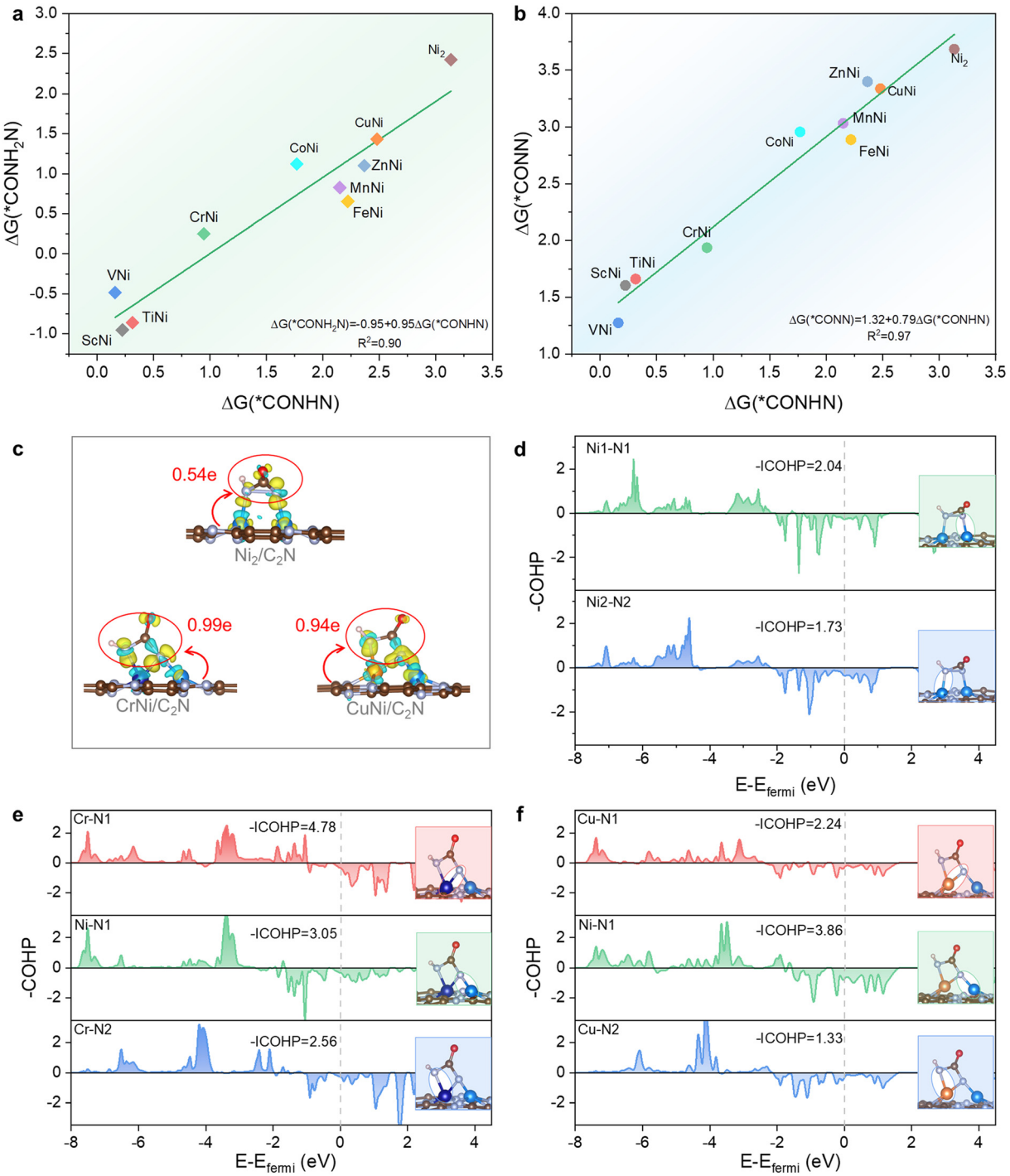

Fig. 4 The linear relationship between the adsorption free energy of *CONHN and *$CONH_2NH$ (a) and between that of *CONHN and *CONN (b) on all TMNi sites of TMNi/C_2N. (c) The charge density difference between *CONHN and TM/C_2N (TM = Ni, Cr and Cu) and corresponding Bader charge. (d–f) The –COHP of main metal–intermediate bonds on Ni_2/C_2N, $CrNi/C_2N$ and $CuNi/C_2N$, respectively.

Therefore, the analysis of the electronic structure confirms that compared to $CuNi/C_2N$ and Ni_2/C_2N, $CrNi/C_2N$ exhibits a stronger TM–Ni interaction, more noticeable difference in charge distribution, more localized electronic states and higher d-band center. All these merits contribute to the catalyst's stability and the ability of the active center to adsorb and activate UOR intermediates. The distinct electronic structure characteristics of the active center in $CrNi/C_2N$ compared to the other two systems may arise from the pronounced differences in the physicochemical properties between Cr and Ni atoms. On the one hand, the difference in electronegativity between Cr and Ni (1.66 *vs.* 1.91) is more significant than that between Cu and Ni (1.90 *vs.* 1.91), making charge transfer easier. On the other hand, Cr has more unpaired electrons, allowing its spin electrons to localize more easily around Cr after interacting with Ni. Moreover, the 3d electrons of Cr are filled at higher energy levels compared to that of Cu,[39] which allows Cr to enhance its orbital energy level and consequently increase its d-band center through orbital coupling when interacting strongly with Ni.

2.4 Key intermediates of UOR analysis on promising $TMNi/C_2N$

For complex catalytic reactions, it is needed to clarify how active sites influence the adsorption of intermediates from the aspect of the interaction between the active site and key intermediates to understand the effect of active sites on catalytic activity and hence identify the reasons for enhanced activity. The free energy diagrams in Fig. 2e imply that the key steps of the UOR on these three systems involve the deprotonation of the second and fourth protons, with the key species being $*CONH_2NH$, $*CONH_2N$, *CONHN and *CONN. To find a representative species, we employed linear regression analysis to investigate the correlations of adsorption free energies among these species. In Fig. 4a and b and Fig. S5, the adsorption free energies of all *CONHN exhibit strong correlations with $*CONH_2NH$, $*CONH_2N$, and *CONN (the average R^2 value for their linear relationships is 0.91). The average R^2 value between $*CONH_2NH$ and the other three intermediates is 0.87; between $*CONH_2N$ and the others, it is 0.91; and for *CONN, it is 0.87. Based on these results, *CONHN was selected as the key species for subsequent studies of the interactions between adsorbates and adsorption sites.

Next, we examined the adsorption structure of *CONHN and calculated the charge density difference and charge transfer between *CONHN and the three catalysts. As depicted in Fig. 4c, in the Ni_2/C_2N system, due to the homogeneity and symmetry of the metal atom pair, *CONHN tends to have its two N atoms positioned atop the two Ni, forming two Ni–N bonds. In contrast, the heterogeneity of the metal atom pairs in $CrNi/C_2N$ and $CuNi/C_2N$ leads to the N atom (denoted as N1) in *CONHN that does not connect with H adsorbing at the TM–Ni bridge site, while the N atom (denoted as N2), which connects with H, adsorbing at the top site of TM, thus forming two TM–N bonds (*i.e.* TM–N1 and TM–N2) and one Ni–N2 bond. This leads to stronger bonding between *CONHN and the CrNi and CuNi centers compared to that between *CONHN and Ni_2. The charge density difference in Fig. 4c reveals significant charge transfer between *CONHN and the metal centers through TM–N bonds. Notably, for Ni_2/C_2N, due to the higher electronegativity of N compared to Ni, charge accumulation occurs around N, while charge depletion is observed around Ni, indicating that Ni transfers electrons to N. Furthermore, the charge transfer from Ni to N1 is more pronounced than from Ni to N2, suggesting that N1 acquires more electrons from Ni, resulting in a stronger Ni–N1 interaction compared to the Ni–N2 interaction. Similar behavior is observed in the $CrNi/C_2N$ and $CuNi/C_2N$ systems, where electrons are transferred from the bimetallic centers to *CONHN, with N2 in *CONHN receiving more electrons than N1 from the bimetallic centers. In $CrNi/C_2N$, electrons are primarily transferred from Cr to both N1 and N2, while in $CuNi/C_2N$, Cu donates electrons to N1, and both Cu and Ni transfer electrons to N2. Comparing the charge density difference of the three systems, there is more significant charge transfer between the CrNi or CuNi center and *CONHN compared to the transfer between Ni_2 and *CONHN. The calculated Bader charge indicates that the amount of charge transferred to *CONHN from the three systems ($CrNi/C_2N$, $CuNi/C_2N$, and Ni_2/C_2N) is 0.99, 0.94, and 0.54 e, respectively. This confirms that $CrNi/C_2N$ and $CuNi/C_2N$ transfer more electrons to *CONHN, suggesting a stronger interaction between $CrNi/C_2N$, $CuNi/C_2N$, and *CONHN than that between Ni_2/C_2N and *CONHN.

To further validate the results and investigate which of the $CrNi/C_2N$ or $CuNi/C_2N$ exhibits a stronger interaction with *CONHN, we calculated the –COHP of N1 and N2 with the bimetallic centers of the three systems. From these calculations, we derived the –ICOHP values, which provide a quantitative assessment of bond strength (Fig. 4d–f). For the Ni_2/C_2N system, the bonding contribution of Ni1–N1 is greater than that of Ni2–N2, while its antibonding contribution is smaller than that of Ni2–N2. This strengthens the conclusion that the Ni1–N1 interaction is more robust, and the –ICOHP values reinforce that Ni1–N1 has a stronger bonding effect than Ni2–N2. This finding aligns with the previous charge transfer analysis. For the $CrNi/C_2N$ system, a similar phenomenon is observed, where the bonding contribution between Cr–N1 and Ni–N1 is significantly larger than that between Cr–N2. The –ICOHP value for Cr–N1 reaches 4.78, which is substantially higher than those for Ni–N1 (3.05) and Cr–N2 (2.56). This indicates that the strong interaction between $CrNi/C_2N$ and *CONHN primarily originates from the Cr–N1 bond. In the $CuNi/C_2N$ system, the bonding contributions for both Ni–N1 and Cu–N1 are notably higher than for Cu–N2, and the order of –ICOHP values is as follows: Ni–N1 (3.85) > Cu–N1 (2.24) > Cu–N2 (1.33). It suggests that the strong interaction between $CuNi/C_2N$ and *CONHN arises from the contributions of both metals

interacting with N1, which is also consistent with the charge transfer analysis.

Furthermore, comparing the –ICOHP values across the three systems reveals that the metal–N bonds in the CrNi/C_2N system are stronger than those in the CuNi/C_2N system, while the metal–N bonds in the Ni_2/C_2N system are the weakest. These data confirm that the interaction between CrNi/C_2N and *CONHN is the strongest, followed by CuNi/C_2N, and the last is Ni_2/C_2N. The analysis of the interaction between the metal centers and *CONHN indicates that the inclusion of Cr or Cu enhances the adsorption of key UOR intermediates on the bimetallic centers of TMNi/C_2N. Notably, Cr is most effective at strengthening the interaction between the metal center and N-containing intermediates, thereby facilitating the adsorption of key intermediates and promoting their conversion. This finding aligns with the free energy analysis of the UOR (Fig. 2).

Combining these results with the electronic structure analysis, we can understand why CrNi/C_2N favors intermediates adsorption. Firstly, the relatively low electronegativity of Cr and the presence of more unpaired electrons in the Cr–Ni active center allow for easier electron donation, facilitating the capture of N-containing intermediates which have higher electronegativity. Moreover, the significant differences in spin moments between the Cr–Ni active centers enhance their ability to adsorb and activate intermediates, leading to a noticeable spin moment change in key species after adsorption (Fig. S6). Lastly, the higher d-band center of the Cr–Ni active center also favors the adsorption of intermediates. Therefore, these results and analyses demonstrate that the unique electronic structure of the CrNi/C_2N system is beneficial for the adsorption and conversion of reaction intermediates, resulting in higher UOR activity.

2.5 The selectivity of promising TMNi/C_2N

The selectivity of catalysts is one of the key indicators of catalytic performance, and a good catalyst should exhibit high selectivity. In most case, the OER is one of the competing reactions for the UOR. To explore the likelihood that CrNi/C_2N and CuNi/C_2N preferentially undergo the UOR over the OER, we calculated the free energy changes of the OER (Fig. S7) on the bimetallic centers of the CrNi/C_2N and CuNi/C_2N and obtained their limiting potentials. In Fig. 5a, the PDS for the OER on both CrNi/C_2N and CuNi/C_2N is the third step, that is, the conversion of *O to *OOH, with ΔG_{PDS} of 2.87 eV and 2.15 eV, respectively. Accordingly, their

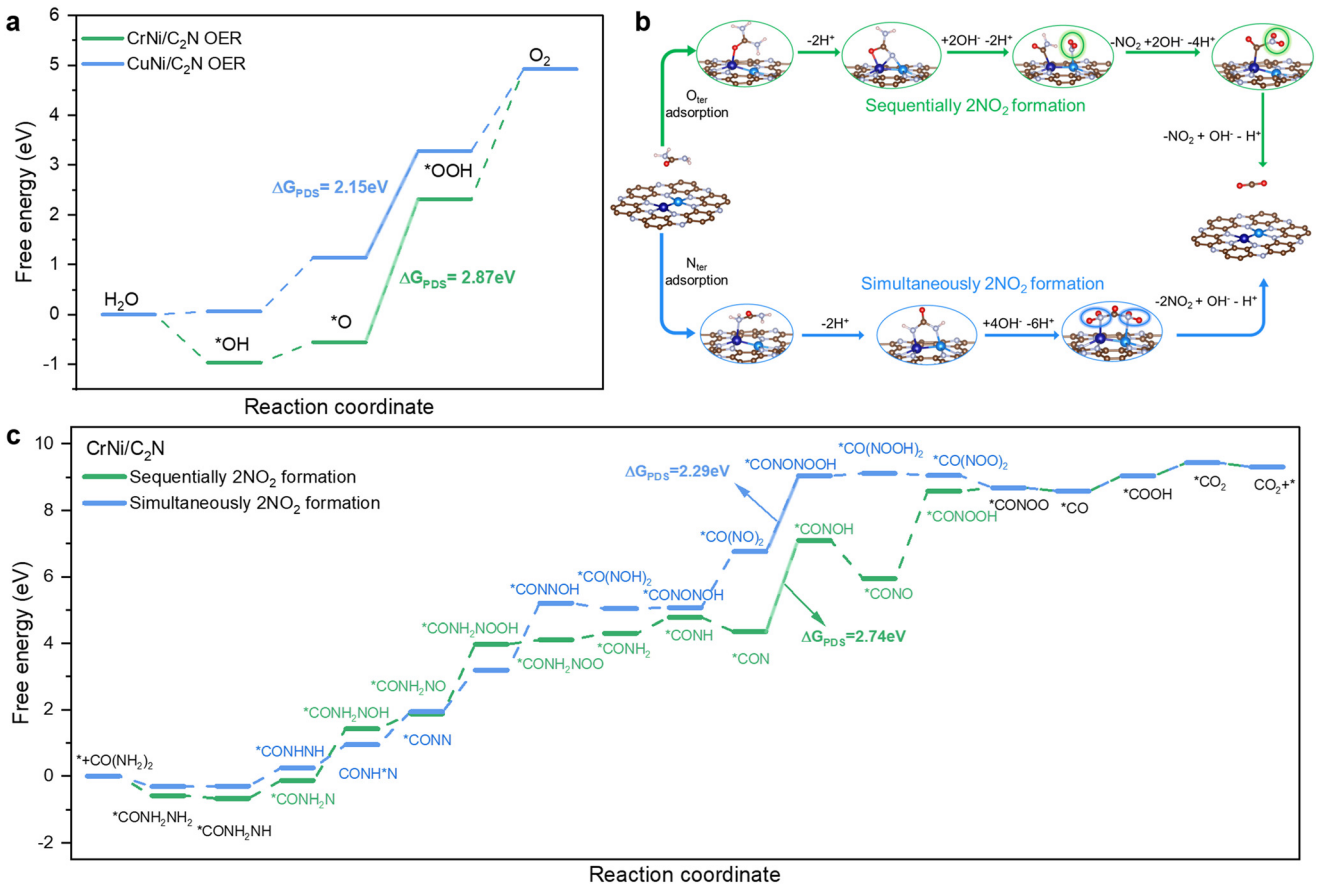

Fig. 5 (a) The free energy diagrams of the OER on CrNi/C_2N and CuNi/C_2N. (b) The main process of urea oxidation to produce $2NO_2$ sequentially and simultaneously on CrNi/C_2N. (c) The free energy diagrams of urea oxidation to produce $2NO_2$ sequentially and simultaneously on CrNi/C_2N.

corresponding limiting potentials are 2.87 V and 2.15 V *vs.* RHE, respectively. Based on our discussion in section 2.2, when limiting potentials of 0.99 V and 1.08 V are applied for $CrNi/C_2N$ and $CuNi/C_2N$ systems, respectively, electrochemical UOR on $CrNi/C_2N$ and $CuNi/C_2N$ becomes spontaneous. The differences in the limiting potentials of the OER and UOR for $CrNi/C_2N$ and $CuNi/C_2N$ systems are 1.88 V and 1.07 V, respectively, so it is difficult for both $CrNi/C_2N$ and $CuNi/C_2N$ to experience the competing OER, and that $CrNi/C_2N$ is less likely to undergo the OER than $CuNi/C_2N$.

In addition to the OER, UOR catalysts at high potentials may also produce undesirable NO*x* species and their acid ions, particularly NO_2, NO_2^- or NO_3^- through over-oxidation.[40–42] To investigate the potential formation of NO_2, we calculated the free energy change for NO_2 production during the UOR on $CrNi/C_2N$. Based on the adsorption modes of urea analyzed before (O_{ter} and N_{ter}), we considered two pathways for NO_2 formation: one pathway starts from urea adsorbed in the O_{ter} mode and sequentially generates NO_2, while the other starts from urea in the N_{ter} mode and produces NO_2 simultaneously. The sketch of reaction pathways is shown in Fig. 5b, with the calculated free energy change (Fig. 5c). For the pathway that forms NO_2 sequentially, the PDS corresponds to the third hydroxylation step of nitrogen, *i.e.*, the transition from *CON to *CONOH, with ΔG_{PDS} of 2.74 eV. In contrast, for the simultaneous generation of the NO_2 pathway, the PDS is also the third hydroxylation step of nitrogen, *i.e.*, from $*CO(NO)_2$ to *CONONOOH, with ΔG_{PDS} of 2.29 eV. Both pathways have ΔG_{PDS} that are significantly higher than that for the UOR pathway generating N_2 (>1.20 eV).

Besides, the urea oxidation to formation of NO_2^- and NO_3^- can also compete with the N_2 formation. Then, we computed the free energy profiles for competing pathways leading to NO_2^- and NO_3^- on $CrNi/C_2N$, following the mechanism proposed by Chen *et al.*[42] The free energy profiles are shown in Fig. S8. The PDS is *NO oxidation to *NOOH for the NO_2^- formation pathway with ΔG_{PDS} of 2.00 eV, and is *NOO oxidation to *NOOOH for the NO_3^- formation with ΔG_{PDS} of 2.08 eV. These two competing pathways need more energy (at least 1 eV) to overcome the N_2 generation pathway, indicating the priority of the N_2 formation pathway.

These indicate that in the $CrNi/C_2N$ system, the hydroxylation of N-containing intermediates of the UOR is difficult, and the overoxidation to produce NO_2, NO_2^- or NO_3^- is also challenging. Consequently, the production of UOR by-products is minimized, contributing to higher selectivity for the N_2 product on $CrNi/C_2N$. Based on the above analysis, we concluded that $CrNi/C_2N$, which exhibits the highest UOR activity among all constructed $TMNi/C_2N$, demonstrates a high selectivity for N_2 production during the UOR and is less susceptible to competing with the OER.

2.6 Guidelines for the experimental feasibility of promising $TMNi/C_2N$

Many strategies have been developed to synthesize well-defined bimetallic single-atom catalysts.[43,44] Based on these strategies, several catalysts with structures similar to $TMNi/C_2N$, such as dual metal atoms on polymeric carbon nitride (M1M2/PCN, M1 = Zn/Co/Ni/Bi, M2 = Ru/Cu),[45] FeNi atom pairs embedded in nitrogen-doped carbon (FeNiNC),[46] FeCu pairs on carbon substrate,[44] PtNi on C_3N_4 (ref. 47) have been synthesized. Therefore, the applicability of these strategies can provide valuable guidance for achieving the experimental feasibility of the predicted $CrNi/C_2N$ catalyst. Additionally, the thermal stability of the $CrNi/C_2N$ catalyst was evaluated using AIMD simulations at 500 K. In Fig. 6, the structure remained very stable during the dynamical simulations, with no significant structural deformation observed at 500 K. This clearly indicates the high thermal stability of the $CrNi/C_2N$ catalyst. Therefore, it is anticipated that the successful synthesis of the $CrNi/C_2N$ catalyst can be achieved in the future.

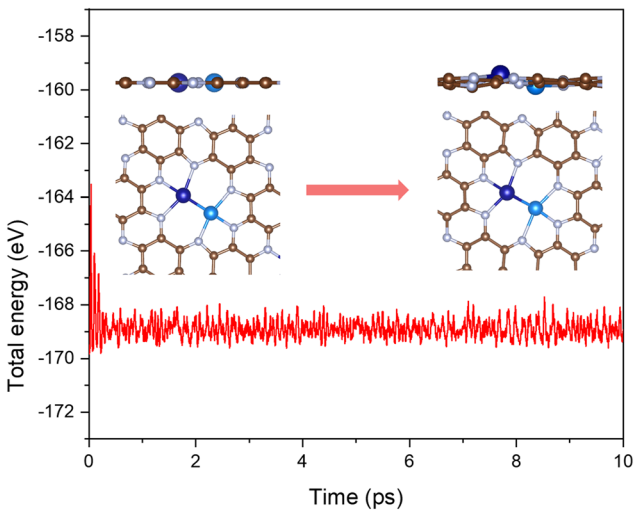

Fig. 6 The total energy of $CrNi/C_2N$ during AIMD simulation at 500 K for 10 ps and the corresponding structure before and after the simulation.

3 Conclusions

In this work, we designed a series of stable 3d transition metal heterometal atom pairs (TMNi) supported on C_2N through DFT calculations, systematically investigating their potential to enhance the activity of Ni_2/C_2N. Our results demonstrate that all examined TM atoms can improve urea adsorption at the metallic pair active centers of $TMNi/C_2N$. Notably, $CrNi/C_2N$ and $CuNi/C_2N$ emerged as promising electrocatalysts for the UOR, exhibiting superior catalytic activity in both the O_{ter} and the N_{ter} pathways, significantly surpassing their homonuclear counterparts. Among these, both $CuNi/C_2N$ and $CrNi/C_2N$ prefer the N_{ter} pathway, with $CrNi/C_2N$ displaying a superior capability to lower the limiting potential of the UOR compared to $CuNi/C_2N$. In these systems, either the second or the fourth proton desorption step represents the rate-determining step, and

we identify *CONHN as the key intermediate by correlating the ΔG_{ads} of relevant intermediates. Further analysis of charge transfer, spin density, and bonding/antibonding orbital populations indicates that the CrNi center significantly enhances UOR activity by improving the adsorption of key intermediates compared to the CuNi center. The enhanced catalytic performance of Cr in the TMNi/C_2N system primarily stems from the stronger TM–Ni interactions, notable differences in charge distribution, more localized electronic states, and a higher d-band center associated with CrNi/C_2N relative to CuNi/C_2N and Ni_2/C_2N. These attributes not only ensure the stability of the well-dispersed CrNi pairs on C_2N but also amplify the ability of the active center to adsorb and activate UOR intermediates. Moreover, CrNi/C_2N demonstrates good selectivity for N_2 production during the UOR by exhibiting reduced susceptibility to forming NO_2, NO_2^- and NO_3^- by-product and undergoing the competing OER. Thus CrNi/C_2N is identified as a highly effective catalyst for the UOR, which has the possibility to be produced and verified by experiment. This study provides a comprehensive understanding of the catalytic activity of TMNi/C_2N and highlights the exceptional potential of CrNi/C_2N as a highly efficient electrocatalyst for the UOR, offering guidance for advanced catalyst design through the strategic use of transition metal heterometal atom pairs.

4 Theoretical details

Density functional theory (DFT) calculations with spin polarization correction were conducted using the Vienna *Ab initio* Simulation Package (VASP). The projected augmented wave (PAW) method was utilized, and the generalized gradient approximation (GGA) implemented by the Perdew–Burke–Ernzerhof (PBE) functional was adopted to incorporate the exchange–correlation functional.[48–51] A 5 × 5 × 1 Monkhorst–Pack *K*-point mesh was sampled in the Brillouin zone, with a cutoff energy set to 450 eV for geometric optimization. The convergence criteria were 10^{-5} eV in energy between two electronic steps and 0.01 eV $Å^{-1}$ for the forces acting on each atom.[52] van der Waals effect was included using Grimme's DFT-D3 correction method during optimization.[53] To evaluate the stability of the catalysts, *ab initio* molecular dynamics (AIMD) simulations were carried out in an NVT ensemble for 10 ps with a time step of 1.0 fs, with temperature controlled by the Nosé–Hoover method.[54]

One unit cell of C_2N contains 12 carbon atoms and 6 nitrogen atoms with a lattice parameter of 8.33 Å.[55] The C_2N slab model was created by adding a vacuum layer of 18 Å thickness in the vertical direction of the C_2N layer to prevent spurious interactions. The TMNi/C_2N was constructed by adding the TM–Ni pair in the hole of the C_2N layer. The adsorption energy (ΔE_{ads}) of each intermediate of the UOR and the Gibbs free energy change (ΔG) of each step of the UOR were calculated according to our previous method (or see the SI).[27]

Conflicts of interest

The authors declare no competing financial interest.

Data availability

The data supporting this article have been included as part of the supplementary information (SI).

Supplementary information: the UOR free energy diagrams of all systems, relative figures of charge density difference and spin density, adsorption structure of OER intermediates and free energy diagram of by-prouducts formation have been included as part of the SI. See DOI: https://doi.org/10.1039/d5im00252d.

Acknowledgements

This work was financially supported by the National Natural Science Foundation of China (No. 52200076), the Special Research Fellowship of the Chinese Academy of Science (No. E3296201), the Research Foundation of Chongqing University of Science and Technology (No. ckrc2022015), and the Natural Science Foundation of Chongqing (No. CSTB2025NSCQ-GPX0920). In addition, DFT calculations in this work have been performed at the Hefei Advanced Computing Center, China.

References

1 D. D. Zhu, H. Y. Zhang, J. H. Miao, F. X. Hu, L. Wang, Y. J. Tang, M. Qiao and C. X. Guo, Strategies for designing more efficient electrocatalysts towards the urea oxidation reaction, *J. Mater. Chem. A*, 2022, **10**, 3296–3313.
2 B. K. Boggs, R. L. King and G. G. Botte, Urea electrolysis: Direct hydrogen production from urine, *Chem. Commun.*, 2009, 4859–4861.
3 H. Wang, X. Zheng, L. Fang and S. Lu, Urea electrooxidation in alkaline environment: Fundamentals and applications, *ChemElectroChem*, 2023, **10**, e202300138.
4 X. Zheng, J. Yang, P. Li, Z. Jiang, P. Zhu, Q. Wang, J. Wu, E. Zhang, W. Sun, S. Dou, D. Wang and Y. Li, Dual-atom support boosts nickel-catalyzed urea electrooxidation, *Angew. Chem., Int. Ed.*, 2023, **62**, e202217449.
5 G. Zhan, L. Hu, H. Li, J. Dai, L. Zhao, Q. Zheng, X. Zou, Y. Shi, J. Wang and W. Hou, Highly selective urea electrooxidation coupled with efficient hydrogen evolution, *Nat. Commun.*, 2024, **15**, 5918.
6 W. Ge, L. Lin, S.-Q. Wang, Y. Wang, X. Ma, Q. An and L. Zhao, Electrocatalytic urea oxidation: advances in mechanistic insights, nanocatalyst design, and applications, *J. Mater. Chem. A*, 2023, **11**, 15100–15121.
7 Z. Li, Y. Zheng, H. Guo, X. Cheng, Y. Huang, C. Liu, J. Zang and L. Dong, Ni-based electrocatalysts for urea oxidation reaction: Mechanistic insights and recent advancements, *J. Alloys Compd.*, 2024, **1008**, 176591.
8 Y. Zhang, Y. Lei, Y. Yan, W. Cai, J. Huang, Y. Lai and Z. Lin, Enhancing hydrogen production capability from urine-

containing sewage through optimization of urea oxidation pathways, *Appl. Catal., B*, 2024, **353**, 124064.
9 L. Sun, X. Li, J. Li, Y. Zeng and S. Lu, Understanding orbital hybridizations of nickel-based catalysts for urea electrooxidation: Opportunities and challenges, *Energy Fuels*, 2025, **39**, 13969–13996.
10 S. Lu, X. Zheng, Y. Zeng, Q. Hua, X. Wang, Y. Liu and H. Liu, Triphenylamine-substituted Ni (II) porphyrins for urea electro-oxidation, *Inorg. Chem.*, 2024, **63**, 20929–20934.
11 S. W. Tatarchuk, J. J. Medvedev, F. Li, Y. Tobolovskaya and A. Klinkova, Nickel-catalyzed urea electrolysis: From nitrite and cyanate as major products to nitrogen evolution, *Angew. Chem., Int. Ed.*, 2022, **61**, e202209839.
12 X. Gao, P. Wang, X. Sun, M. Jaroniec, Y. Zheng and S.-Z. Qiao, Membrane-free water electrolysis for hydrogen generation with low cost, *Angew. Chem., Int. Ed.*, 2025, **64**, e202417987.
13 S. T. P. N. Kment, A. Bakandritsos, I. Tantis, H. Kmentová, Y. Zuo, O. Henrotte, A. Naldoni, M. Otyepka, R. S. Varma and R. Zbořil, Single atom catalysts based on earth-abundant metals for energy-related applications, *Chem. Rev.*, 2024, **124**, 11767–11847.
14 J. Luo, G. I. Waterhouse, L. Peng and Q. Chen, Recent progress in high-loading single-atom catalysts and their applications, *Ind. Chem. Mater.*, 2023, **1**, 486–500.
15 Z. Yang, R. Chen, L. Zhang, Y. Li and C. Li, Recent progress in nickel single-atom catalysts for the electroreduction of CO_2 to CO, *Ind. Chem. Mater.*, 2024, **2**, 533–555.
16 R. Li and D. Wang, Superiority of dual-atom catalysts in electrocatalysis: One step further than single-atom catalysts, *Adv. Energy Mater.*, 2022, **12**, 2103564.
17 G. Sun, Z.-J. Zhao, R. Mu, S. Zha, L. Li, S. Chen, K. Zang, J. Luo, Z. Li and S. C. Purdy, Breaking the scaling relationship via thermally stable Pt/Cu single atom alloys for catalytic dehydrogenation, *Nat. Commun.*, 2018, **9**, 4454.
18 A. Pedersen, J. Barrio, A. Li, R. Jervis, D. J. L. Brett, M. M. Titirici and I. E. L. Stephens, Dual-metal atom electrocatalysts: Theory, synthesis, characterization, and applications, *Adv. Energy Mater.*, 2022, **12**, 2102715.
19 K. Liu, J. Li, Y. Liu, M. Wang and H. Cui, Dual metal atom catalysts: Advantages in electrocatalytic reactions, *J. Energy Chem.*, 2023, **79**, 515–534.
20 J. Gu, J. Wang and J. Leszczynski, Co and Ni single sites on the (111) n surface of γ-Al_2O_3–a periodic boundary DFT study, *Ind. Chem. Mater.*, 2023, **1**, 117–128.
21 J. Xie, J. Du, P. Chen, G. Wang, J. Zhang, X. Yang, A. Kong and F. Yu, A facile route of Ti decoration for modulating M–O–Ti (M = Ni, Co) and oxygen vacancies on NiCo-LDH electrocatalysts for efficient oxygen evolution reaction, *Ind. Chem. Mater.*, 2025, **3**, 342–352.
22 J. Mahmood, E. K. Lee, M. Jung, D. Shin, I. Y. Jeon, S. M. Jung, H. J. Choi, J. M. Seo, S. Y. Bae, S. D. Sohn, N. Park, J. H. Oh, H. J. Shin and J. B. Baek, Nitrogenated holey two-dimensional structures, *Nat. Commun.*, 2015, **6**, 6486.
23 F. Li and Z. Chen, Cu dimer anchored on C_2N monolayer: Low-cost and efficient Bi-atom catalyst for CO oxidation, *Nanoscale*, 2018, **10**, 15696–15705.
24 D. Jiao, Y. Tian, H. Wang, Q. Cai and J. Zhao, Single transition metal atoms anchored on a C_2N monolayer as efficient catalysts for hydrazine electrooxidation, *Phys. Chem. Chem. Phys.*, 2020, **22**, 16691–16700.
25 Y. Ying, K. Fan, X. Luo, J. Qiao and H. Huang, Unravelling the origin of bifunctional OER/ORR activity for single-atom catalysts supported on C_2N by DFT and machine learning, *J. Mater. Chem. A*, 2021, **9**, 16860–16867.
26 Z. Sun, X. Luo, H. Shang, Z. Wang, L. Zhang and W. Chen, Atomic printing strategy achieves precise anchoring of dual-copper atoms on C_2N structure for efficient CO_2 reduction to ethylene, *Angew. Chem.*, 2024, **136**, e202405778.
27 X. Zheng and S. Lu, Theoretical exploration of anchoring type effects of C_2N nanosheet-supported nickel atoms for urea electrooxidation, *ACS Appl. Nano Mater.*, 2024, **7**, 3361–3372.
28 X. Zhao, F. Wang, X.-P. Kong, R. Fang and Y. Li, Dual-metal hetero-single-atoms with different coordination for efficient synergistic catalysis, *J. Am. Chem. Soc.*, 2021, **143**, 16068–16077.
29 W. Ren, X. Tan, W. Yang, C. Jia, S. Xu, K. Wang, S. C. Smith and C. Zhao, Isolated diatomic Ni-Fe metal–nitrogen sites for synergistic electroreduction of CO_2, *Angew. Chem., Int. Ed.*, 2019, **58**, 6972–6976.
30 Y. Ouyang, L. Shi, X. Bai, Q. Li and J. Wang, Breaking scaling relations for efficient CO_2 electrochemical reduction through dual-atom catalysts, *Chem. Sci.*, 2020, **11**, 1807–1813.
31 X. Zheng, J. Yang, P. Li, Z. Jiang, P. Zhu, Q. Wang, J. Wu, E. Zhang, W. Sun, S. Dou, D. Wang and Y. Li, Dual-atom support boosts nickel-catalyzed urea electrooxidation, *Angew. Chem., Int. Ed.*, 2023, **62**, e202217449.
32 Y. Chen, J. Meng, M. Xu, L. Qiao, D. Liu, Y. Kong, X. Hu, Q. Liu, M. Chen, S. Lyu, R. Tong and H. Pan, Adaptive active site turning for superior OER and UOR on Ir-Ni_3N catalyst, *Adv. Funct. Mater.*, 2025, **35**, 2413474.
33 K. Mathew, R. Sundararaman, K. Letchworth-Weaver, T. A. Arias and R. G. Hennig, Implicit solvation model for density-functional study of nanocrystal surfaces and reaction pathways, *J. Chem. Phys.*, 2014, **140**, 084106.
34 X. Guo, J. Gu, S. Lin, S. Zhang, Z. Chen and S. Huang, Tackling the activity and selectivity challenges of electrocatalysts toward the nitrogen reduction reaction via atomically dispersed biatom catalysts, *J. Am. Chem. Soc.*, 2020, **142**, 5709–5721.
35 Z. Fu, C. Fang, S. Liu, A. Cao and J. Yan, Mechanism of potential-dependent CO_2 reduction and H_2 evolution during electrocatalytic CO_2 process, *ACS Catal.*, 2025, **15**, 13507–13515.
36 Z. Li, X. Li, F. Jia, L. Wang and P. Li, Theoretical screening of transition metal atoms supported on two-dimensional Janus VSSe for HER/OER/ORR single-atom catalysts, *J. Mater. Chem. A*, 2025, **13**, 20578–20587.
37 F. Liu, R. Gao, C. Shi, L. Pan, Z.-F. Huang, X. Zhang and J.-J. Zou, Avoiding Sabatier's limitation on spatially correlated Pt–Mn atomic pair sites for oxygen electroreduction, *J. Am. Chem. Soc.*, 2023, **145**, 25252–25263.

38 W. Zhong, Y. Qiu, H. Shen, X. Wang, J. Yuan, C. Jia, S. Bi and J. Jiang, Electronic spin moment as a catalytic descriptor for Fe single-atom catalysts supported on C_2N, *J. Am. Chem. Soc.*, 2021, **143**, 4405–4413.

39 J. K. Nørskov, F. Studt, F. Abild-Pedersen and T. Bligaard, *Fundamental concepts in heterogeneous catalysis*, John Wiley & Sons, 2014.

40 J. Li, J. Li, T. Liu, L. Chen, Y. Li, H. Wang, X. Chen, M. Gong, Z. P. Liu and X. Yang, Deciphering and suppressing over-oxidized nitrogen in nickel-catalyzed urea electrolysis, *Angew. Chem., Int. Ed.*, 2021, **60**, 26656–26662.

41 S. W. Tatarchuk, J. J. Medvedev, A. Klinkova, F. Li, Y. Tobolovskaya and A. Klinkova, Nickel-catalyzed urea electrolysis: From nitrite and cyanate as major products to nitrogen evolution, *Angew. Chem., Int. Ed.*, 2022, **61**, e202209839.

42 S. W. Tatarchuk, R. M. Choueiri, A. J. MacKay, S. J. Johnston, W. M. Cooper, K. S. Snyder, J. J. Medvedev, A. Klinkova and L. D. Chen, Understanding the mechanism of urea oxidation from first-principles calculations, *ChemPhysChem*, 2024, e202300889.

43 J. Zhang, Q.-A. Huang, J. Wang, J. Wang, J. Zhang and Y. Zhao, Supported dual-atom catalysts: Preparation, characterization, and potential applications, *Chin. J. Catal.*, 2020, **41**, 783–798.

44 Y.-X. Zhang, S. Zhang, H. Huang, X. Liu, B. Li, Y. Lee, X. Wang, Y. Bai, M. Sun and Y. Wu, General synthesis of a diatomic catalyst library via a macrocyclic precursor-mediated approach, *J. Am. Chem. Soc.*, 2023, **145**, 4819–4827.

45 Q.-P. Zhao, W.-X. Shi, J. Zhang, Z.-Y. Tian, Z.-M. Zhang, P. Zhang, Y. Wang, S.-Z. Qiao and T.-B. Lu, Photo-induced synthesis of heteronuclear dual-atom catalysts, *Nat. Synth.*, 2024, **3**, 497–506.

46 X. Zhu, D. Zhang, C.-J. Chen, Q. Zhang, R.-S. Liu, Z. Xia, L. Dai, R. Amal and X. Lu, Harnessing the interplay of Fe–Ni atom pairs embedded in nitrogen-doped carbon for bifunctional oxygen electrocatalysis, *Nano Energy*, 2020, **71**, 104597.

47 S. Chen, B. Gong, J. Gu, Y. Lin, B. Yang, Q. Gu, R. Jin, Q. Liu, W. Ying and X. Shi, Dehydrogenation of ammonia borane by platinum-nickel dimers: Regulation of heteroatom interspace boosts bifunctional synergetic catalysis, *Angew. Chem., Int. Ed.*, 2022, **134**, e202211919.

48 G. Kresse and J. Furthmuller, Efficiency of ab-initio total energy calculations for metals and semiconductors using a plane-wave basis set, *Comput. Mater. Sci.*, 1996, **6**, 15–50.

49 P. E. Blochl, Projector augmented-wave method, *Phys. Rev. B*, 1994, **50**, 17953–17979.

50 G. Kresse and D. Joubert, From ultrasoft pseudopotentials to the projector augmented-wave method, *Phys. Rev. B*, 1999, **59**, 1758–1775.

51 J. P. Perdew, K. Burke and M. Ernzerhof, Generalized gradient approximation made simple, *Phys. Rev. Lett.*, 1996, **77**, 3865–3868.

52 H. J. Monkhorst and J. D. Pack, Special points for brillouin-zone integrations, *Phys. Rev. B*, 1976, **13**, 5188–5192.

53 S. Grimme, J. Antony, S. Ehrlich and H. Krieg, A consistent and accurate ab initio parametrization of density functional dispersion correction (DFT-D) for the 94 elements H-Pu, *J. Chem. Phys.*, 2010, **132**, 154104.

54 G. J. Martyna, M. L. Klein and M. E. Tuckerman, Nosé-Hoover chains: The canonical ensemble via continuous dynamics, *J. Chem. Phys.*, 1992, **97**, 2635–2643.

55 S. Chakrabarty, T. Das, P. Banerjee, R. Thapa and G. P. Das, Electron doped CN monolayer as efficient noble metal-free catalysts for CO oxidation, *Appl. Surf. Sci.*, 2017, **418**, 92–98.